Journal of Magnetism and Magnetic Materials 501 (2020) 166405

Contents lists available at ScienceDirect

Journal of Magnetism and Magnetic Materials

journal homepage: www.elsevier.com/locate/jmmm

Research articles

Metamagnetic transition, magnetocaloric effect and electronic structure of the rare-earth anti-perovskite $SnOEu_3$

F. Guillou[a,b,*], D. Paudyal[a], Y. Mudryk[a], A.K. Pathak[a,c], V. Smetana[d], A.-V. Mudring[d], V.K. Pecharsky[a,e]

[a] The Ames Laboratory, U.S. Department of Energy, Iowa State University, Ames, IA 50011-2416, USA
[b] Inner Mongolia Key Laboratory for Physics and Chemistry of Functional Materials, Inner Mongolia Normal University, Hohhot 010022, China
[c] Department of Physics, SUNY Buffalo State, Buffalo, NY 14222, USA
[d] Physical Materials Chemistry, Department of Materials and Environmental Chemistry, Stockholm University, Svante Arrhenius väg 16c, 10691 Stockholm, Sweden
[e] Department of Materials Science and Engineering, Iowa State University, Ames, IA 50011-1096, USA

ARTICLE INFO

Keywords:
Rare-earth alloys
Metamagnetism
Anti-perovskites
Magnetocaloric effect
Band topology
High-pressure

ABSTRACT

Rare-earth anti-perovskites with oxygen are an interesting magnetic materials family at the boundary between intermetallics and oxides, they however remain largely unexplored. Here, magnetic and heat capacity investigations, as well as density functional theory (DFT) calculations, were carried out on $SnOEu_3$. At low magnetic field ($B \leq 0.5$ T), a Néel temperature separates antiferromagnetic and paramagnetic phases at 31 K. When applying higher magnetic field below the Néel temperature, successive transformations toward a ferromagnetic state *via* a number of intermediate canted magnetic structures are observed and are associated with only modest latent heat and transition entropy. High-pressure magnetic measurements confirm the stable divalent state of Eu up to 1.05 GPa. A direct magnetocaloric effect progressively increases with applied magnetic field above the Néel temperature, reaching -16 J kg^{-1} K^{-1} for $\Delta B = 7$ T. On the other hand, the inverse magnetocaloric effect of the field-induced transition below T_N saturates at $\sim+5$ J kg^{-1} K^{-1}. DFT calculations support magnetic instabilities observed experimentally in $SnOEu_3$ and reveal an unusual exchange mechanism and band topology near the Fermi level.

1. Introduction

Although less studied than conventional ABO_3 perovskites, where A is typically a metal cation and B is a metal or metalloid in a six-fold coordination of oxygen [1–3], anti-perovskites – BXA_3 with X representing a non-metallic element such as B, C, N, or O – form an interesting group of materials both from fundamental and applied points of view. In the cubic anti-perovskite structure, the smallest X atoms reside in the centers of octahedra (arranged into a three-dimensional network) made of the larger A atoms, while the B element atoms occupy inter-octahedral voids. $MgCNi_3$, $GaCMn_3$, and related compounds are among the best-known representatives of the anti-perovskite family, owing to their intriguing physical properties: superconductivity, giant magnetoresistance, giant magnetocaloric and/or barocaloric effects, and large negative thermal expansion [4–9]. More recently, lithium-containing anti-perovskites received enhanced attention for their potential in electrochemical applications [10].

Rare earth elements (R) form BXR_3 anti-perovskite structures in combination with X = B, C, N, O, and most of the basic metals B = Al, Ga, In, Sn, Tl, Pb [11–18]. Interestingly, the specific magnetization is particularly high in these compounds, up to ~200 Am^2 kg^{-1}, which renders such materials potentially important for magnetism-related applications such as magnetocaloric materials. While known borides, carbides and nitrides have low magnetic ordering temperatures, the $BOEu_3$ series of compounds stands out. An earlier investigation of the physical properties of $SnOEu_3$ and $InOEu_3$ indicates reasonably high ordering temperatures with an antiferromagnetic order developing at ~30 K for $SnOEu_3$, and a ferromagnetic ordering transition at ~210 K for $InOEu_3$ [15]. Magnetization measurements and X-ray absorption spectroscopy at the Eu L_3 edges support a divalent oxidation state of europium in these compounds [15]. Our study seeks to experimentally and theoretically investigate the magnetism of $SnOEu_3$, with emphasis on the metamagnetic behavior observed when intermediate magnetic fields are applied below the Néel temperature, potentially leading to giant magnetocaloric effect.

* Corresponding author.
E-mail address: francoisguillou@imnu.edu.cn (F. Guillou).

https://doi.org/10.1016/j.jmmm.2020.166405
Received 18 July 2019; Received in revised form 31 December 2019; Accepted 5 January 2020
Available online 07 January 2020
0304-8853/

2. Experimental details

Polycrystalline $SnOEu_3$ samples were synthesized by melting/sintering SnO_2 (powder), Sn (bulk) and Eu in an induction furnace. The high purity europium metal (at least 99.8 at.% pure with respect to all other elements in the periodic table) was prepared by the Materials Preparation Center of the Ames Laboratory. The starting materials weighted in stoichiometric proportions were sealed in a Ta crucible under ~300 mbar He. The sample was first melted at 1200 °C and held at this temperature for 1 h, then cooled to 800 °C over 1/2 h, and annealed at this temperature for 2 h. After this, the crucible was cooled to room temperature by switching the power off. The resulting sample has a shiny grey metallic appearance and is relatively brittle. Exposure to air leads to darkening of the surface within a few hours, small bulk pieces fully decompose within 3–4 days of air exposure. Handling of both Eu metal and the product was performed in a glovebox with purified Ar atmosphere.

Room temperature powder X-ray diffraction (PXRD) characterization was performed on a PANalytical X'PertPro diffractometer employing Cu $K_{\alpha 1}$ radiation and using polyimide Kapton foil to protect the powder from reacting with air. The PXRD patterns were refined by the Rietveld method using FullProf [19]. Single crystal X-ray intensity (SXRD) data (Table 1) were collected using a small (~60 μm) single crystal on a D8 Venture diffractometer (Bruker Inc., Madison, USA; Mo-Kα radiation; λ = 0.71073 Å, Photon 100 CMOS detector) in ω- and φ-scan modes with exposures of 1 s per frame at room temperature (~292 K). The raw frame data were integrated with SAINT [20] and were corrected for absorption using (SADABS) [21]. Initial model of the crystal structure was obtained with SHELXT-2014 [22] and refined using SHELXL-2014 [23], Table 2.

Magnetic and calorimetric measurements were carried using a physical property measurement system PPMS (Quantum Design) equipped with vibrating sample magnetometer (VSM) and heat capacity options. For magnetization measurements, the sample was weighed in an Ar-filled glovebox and sealed in VSM powder sample holder using Teflon tape. The heat capacity measurements were performed on a small bulk piece (~3 × 3 × 2 mm^3) mounted using Apiezon N grease. Outside the transition region, the measurements were performed with the usual "2τ analysis" using 2% temperature rise and 2τ measurement time. The temperature increment was 0.5 K in the temperature range 2.0–10 K, then 1 K increment between 11 and 70 K, finally 3 K increment above. Complementary experiments coupled to an external analysis were carried out near the magnetic transition by using large single excitation/relaxation pulse [24]. Heat pulses corresponding to a temperature rise of 4 K were targeted, which was found sufficient to fully cover the transition range in zero magnetic field, but only partially covers the transition widths at higher magnetic fields. Even though the magnetic field dependence of heat capacity for "improved puck" is usually considered negligible [25], addenda tables were measured in 2 and 7 T over the temperature range from 2 to 10 K for verification. The magnetic measurements under pressure were carried out in a 7 T magnetic property measurement system MPMS (Quantum Design) magnetometer using a Cu-Be mechanical cell manufactured by HMD (type CC-SPr-8.5D-MC4). The superconducting transition temperature of lead was used as an internal manometer and Daphne oil as pressure transmitting medium. In the investigated pressure range, the temperature expansion of the cell can be neglected in first approximation [26]. The accuracy of the pressure determination by lead has been claimed to be potentially as good as ± 0.015 GPa [26], but might be significantly lower [27].

First-principles electronic structure calculations were performed using the experimental crystallographic parameters, within the local spin density approximation, including Hubbard U [28] and spin-orbit coupling (LSDA + U + SOC), implemented in the full potential linear augmented plane wave (FP-LAPW) band structure methods [29]. Calculations performed with varying U for Eu *4f* show that magnetic moments on Eu *4f* and the total energy of the compound, respectively, increase by 0.07 μ_B and 0.98 eV/f.u. when U is increased from 1 to 4 eV; both become nearly constant when U varies from 4 to 7 eV. The results shown here are those for U = 6.7 eV and an onsite 4*f*-electron exchange parameter J = 0.7 eV (*i.e.*, the observed values for Gd [30]). In addition to representing the region where the magnetic moments and total energy remain nearly constant, the used U and J parameters locate the occupied Eu-4*f* states at ~−2 eV, which agrees well with what is observed for the Eu-4*f* states in the X-ray photoemission spectrum of Eu_2In [31]. The calculated Eu 4*f* and 5*d* orbital moments were about ~0.02 μ_B and those of other atoms are negligible. The k-space integrations have been performed with 16 × 16 × 16 Brillouin zone mesh, which was sufficient for the convergence of total energies and magnetic moments.

Table 1
Details of the single crystal X-ray measurements and data collection of $SnOEu_3$.

Empirical formula	$SnOEu_3$
Formula unit, g mol^{-1}	586.19
Space group	$Pm\bar{3}m$
a, Å	5.074(1)
Volume, $Å^3$	130.62(8)
Z	1
Density (calculated), g/cm^3	7.452
μ, mm^{-1}	39.731
F(0 0 0)	245
θ range, °	4.016–37.921
Index ranges	$-5 \le h \le 5$
	$-6 \le k \le 6$
	$-3 \le l \le 8$
Reflections collected	639
Independent reflections	98
Refinement method	Full-matrix least-squares on F^2
Data/restraints/parameters	98/0/6
Goodness-of-fit on F^2	1.09
Final R indices [$I > 2\sigma(I)$]	$R1$ = 0.018, wR^2 = 0.043
R indices (all data)	$R1$ = 0.031, wR^2 = 0.048
R_{int}	0.024
Largest diff. peak and hole, $e^-/Å^3$	0.96 and −1.01

Table 2
Positions and anisotropic displacement parameters for $SnOEu_3$ with $U_{11} = U_{22}$ and $U_{12} = U_{13} = U_{23} = 0$.

Atom	*Sites*	*x*	*y*	*z*	*Anisotropic displacement parameters*	
					U_{11}	U_{33}
Sn	1*b*	1/2	1/2	1/2	0.0069(2)	0.0069(2)
Eu	3*d*	0	0	1/2	0.0111(3)	0.0041(3)
O	1*a*	0	0	0	0.0058(16)	0.0058(16)

3. Results and discussion

3.1. Assessment of the crystal structure at room temperature

X-ray powder diffraction (PXRD) experiments carried out at room temperature showed that all observed Bragg peaks could be indexed in the cubic space group $Pm\bar{3}m$ (no. 221). Refinement of the PXRD profile leads to lattice parameter of 5.0794(1) Å and cell volume of 131.051(6) $Å^3$ in a reasonable agreement with the original PXRD investigation on $SnOEu_3$ [15].

Single crystal X-ray structure (SXRD) experiments were carried out at room temperature, see Table 1, and their analysis confirmed the cubic anti-perovskite structure for $SnOEu_3$ with cell parameters of a = 5.074(1) Å and V = 130.62(8) $Å^3$. The oxygen occupation is found to be nearly perfectly stoichiometric, *i.e.*, $SnOEu_3$. Anisotropic displacement parameters, presented in Table 2, indicate Eu oblate ellipsoids extended in the direction perpendicular to the Eu-O bond, similar to that observed in $InOEu_3$ by SXRD [15]. Strongly anisotropic

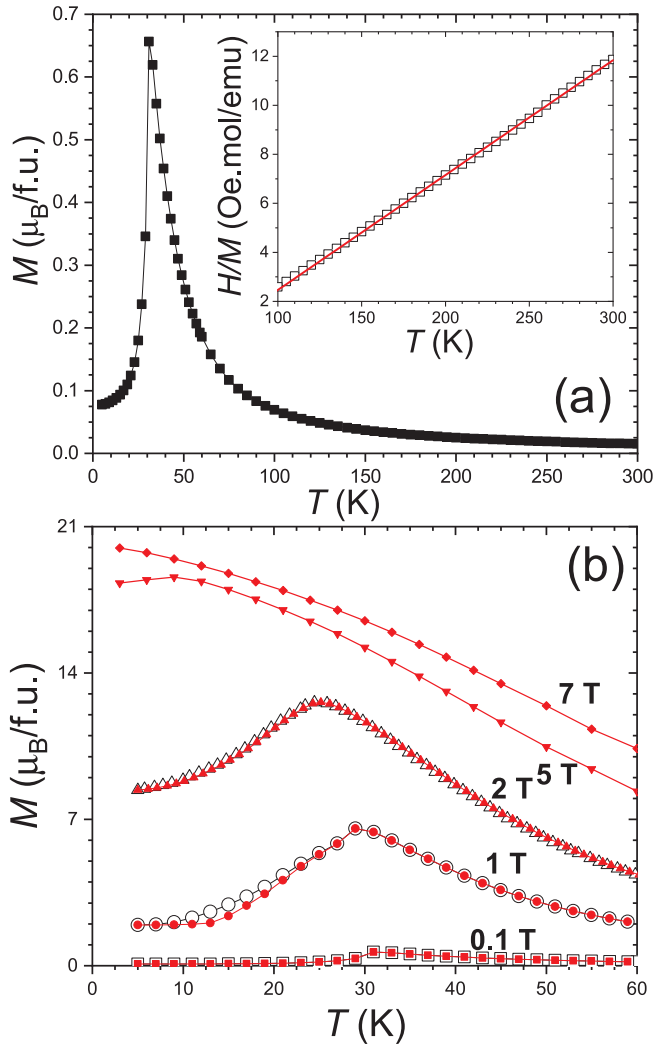

Fig. 1. Magnetic properties of $SnOEu_3$. (a) Magnetization measured as a function of the temperature in $B = 0.1$ T upon cooling, plotted in the inset as the inverse of the susceptibility together with the Curie-Weiss fit. (b) Magnetization measured as a function of the temperature in various field upon cooling (open symbols) and subsequent heating (full symbols).

displacements are frequently observed in conventional ABO_3 perovskites and are often associated with atomic size mismatch prior to distortions. Observing strongly anisotropic displacements is not surprising, since $SnOEu_3$ falls close to the boundary between cubic and orthorhombic anti-perovskites according to a modified Goldschmidt tolerance factor [17].

3.2. Low-field antiferromagnetic ordering and high-field metamagnetism

Fig. 1 illustrates the magnetic properties of $SnOEu_3$ measured over broad ranges of temperature and magnetic fields. Magnetization versus temperature recorded upon cooling at low magnetic field of 0.1 T exhibits a peak typical of an antiferromagnetic ordering with a Néel temperature $T_N \approx 31$ K (taken as the peak maximum). The inverse magnetic susceptibility is linear in the range from 100 to 300 K (inset to Fig. 1a) and a Curie-Weiss fit leads to an effective magnetic moment of 7.6 μ_B/Eu, which is reasonably close to the expected 7.94 μ_B for non-interacting Eu^{2+} ions. The Weiss temperature $\theta_W \approx 48$ K is positive despite the antiferromagnetic ordering, suggesting strong underlying ferromagnetic interactions. Application of larger magnetic fields still shows a magnetization maximum up to at least 5 T (Fig. 1b) but shifting toward lower temperatures and broadening with the increase of the

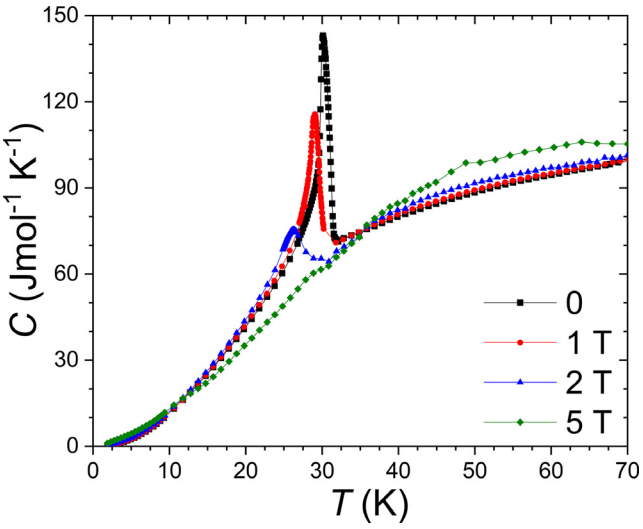

Fig. 2. Heat capacity of $SnOEu_3$ in zero magnetic field (squares), 1 T (circles), 2 T (triangles) and 5 T (diamonds), measurements were performed upon warming after a zero-field cooling.

magnetic field. Above 31 K, high magnetization values – larger than expected for a paramagnet – develop with the magnetic field, suggesting that high-magnetic field in concert with underlying ferromagnetic interactions lead to a stabilization of a ferromagnetic structure, which is initially non-collinear. A high-field ferromagnetic phase agrees with the shape of the $M(T)$ curve in 7 T. Due to the broadening of magnetic transitions in finite magnetic fields, only an indistinct inflection point is observed around ~40 K. When ferromagnetism is further stabilized by external pressure (Section 3.4), this inflection point becomes clearer and suggests a high-field ferromagnetic transition with a Curie temperature of ~50 K in 1.05 GPa.

Heat capacity measurements are shown in Fig. 2. In zero magnetic field, a heat capacity peak clearly marks out the antiferromagnetic transition around 31 K; its λ-shape suggests of a second-order transition in $B = 0$, in line with the absence of thermal hysteresis on low-field $M(T)$ curves. With the increase in magnetic field, the heat capacity anomaly shifts to lower temperature and is progressively broadened out until no clear signature of the magnetic transition can be distinguished in $B = 5$ T. On the other hand, at low temperatures ($T < 15$ K), the $C(T)$ curves in $B = 1$ T and 2 T practically overlap with the heat capacity measured in $B = 0$, but the heat capacity measured in $B = 5$ T is significantly larger compared to heat capacity in $B = 0$. Apparently, the entropy and, in particular, its magnetic contribution is strongly redistributed with the application of finite magnetic fields.

To illustrate the importance of the application of the magnetic field on the magnetic states observed below 31 K, Fig. 3 presents in parallel measurements of the magnetization and heat capacity as a function of the magnetic field at $T \approx 3$ K. It is worth noting that measurements of the heat capacity as a function of magnetic field are not completely isothermal as one has to apply small temperature rises (δT_{rise}) to record the heat capacity. Yet, by applying only a small δT_{rise} of 0.02 K, *i.e.* less than 1% of the absolute temperature, to the platform one can neglect this matter in first approximation.

A striking correlation is observed between the field dependence of the magnetization $M(B)$ and heat capacity $C(B)$. The application of increasing magnetic fields at $T = 3$ K leads to a linear increase in magnetization up to ~1 T, then the development of two successive magnetization jumps: one step-like at ~1.25 T and the second separated from the first by a small plateau, broader, centered at 2.6 T; a third anomaly corresponding to a rather smooth increase is centered around 5.5 T, before to reach a final saturation plateau. At 7 T, the magnetization saturates around 20.5 μ_B/f.u., close to the $3gJ(Eu^{2+}) = 21$ μ_B/

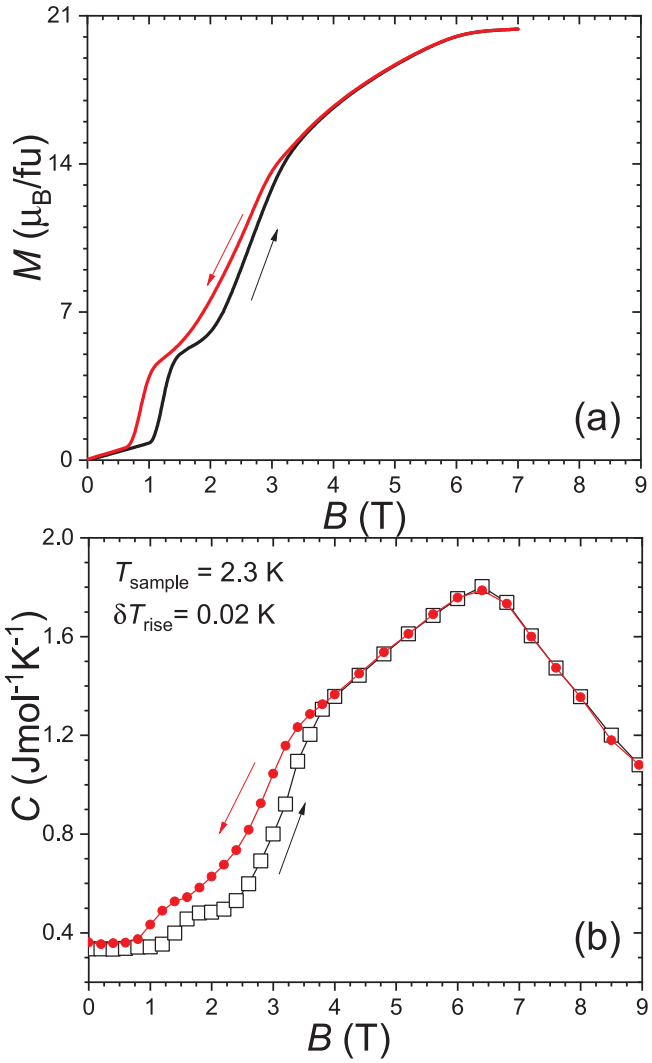

Fig. 3. Field dependence of the magnetization at $T = 3$ K and the heat capacity at $T = 2.3$ K in $SnOEu_3$ (both after zero field cooling) measured upon magnetizing and demagnetizing.

f.u. expected for Eu^{2+} (where g is the Landé factor and J is the total angular momentum). Upon demagnetizing, the $M(B)$ curve shows the same overall shape but is slightly shifted toward lower magnetic fields with a hysteresis of ~0.4 T at the step-like magnetization transitions. Below 0.6 T the demagnetization and magnetization data overlap, indicating that the material fully returns into its zero-field antiferromagnetic state. The combination of discontinuous magnetization jumps and magnetic hysteresis highlights the first-order character of the metamagnetic transition(s). Both low-field antiferromagnetism and high-field metamagnetism are in line with the original report on $SnOEu_3$ [15].

Away from magnetic phase transitions, the application of a magnetic field usually decreases the heat capacity due to the quenching of the magnetic contribution. In contrast, $SnOEu_3$ shows an unexpected increase in heat capacity with the magnetic field, until approaching magnetic saturation around $B = 6$ T. Upon magnetizing, the range of constant magnetic susceptibility at $B < 1.1$ T corresponding to the antiferromagnetic ground state is not associated with any significant thermal response. Once the magnetic field exceeds 1.1 T, two consecutive metamagnetic jumps occur, and, correspondently, the heat capacity also increases mimicking the behavior of magnetization. Not only the critical magnetic fields where the metamagnetic jumps are observed are similar for magnetization and heat capacity data (a slightly higher critical field on the $C(B)$ curve is likely observed due to a larger demagnetization factor of the flat heat capacity sample), but also the magnetic hysteresis and the overall succession of two sharp jumps and a broad increase are identical. While metamagnetic transitions are generally observed in collinear antiferromagnets with significant uniaxial magnetic anisotropy, the combination of low field metamagnetic jump and a progressive saturation at higher field is more typical of materials with limited magnetic anisotropy energy [32], as expected for cubic $SnOEu_3$ containing s-state Eu^{2+}. Though uncommon, observing discontinuities in the field dependence of the heat capacity at low temperatures (significantly below the magnetic transition) is not unique to $SnOEu_3$ and has also been reported for other materials experiencing first-order "metamagnetic" transitions, for instance: i) in $Pr_{1-x}Ca_xMnO_3$ combining a competition between different magnetic orders, orbital ordering, and phase separation phenomena [33]; ii) in Laves phases like $Er_{1-x}Y_xCo_2$ presenting a succession of spin reorientation and ferrimagnetic transitions [34]; or iii) in the prototypical Gd_5Ge_4 magnetocaloric material experiencing a particularly strong first-order transition [35]. In all these examples the application of a magnetic field induces a transition from an antiferromagnetic toward a ferro- or ferrimagnetic state, which results in a discontinuous decrease in heat capacity, while in contrast, the heat capacity increases in $SnOEu_3$. Once the fully collinear ferromagnetic phase is induced above ~6 T at $T = 3$ K, the heat capacity decreases as a result of the suppression of the ferromagnetic spin-waves contribution.

To reveal additional details about the metamagnetic transitions, the isothermal magnetization was systematically examined between 3 and 70 K (Fig. 4(a) below T_N and (b) above T_N). As anticipated for a metamagnetic transition from an antiferromagnetic state toward a higher magnetization state [32], increasing the temperature leads to a shift of the magnetization jumps to lower magnetic field. The jumps widen over larger field ranges, until the Néel temperature around 31 K is reached, where the metamagnetism disappears. Above this temperature, magnetization curves remain non-linear, non-linearity vanishing with the increase in temperature (Fig. 4(b)). Taking the derivatives of the $M(B)$ curves revealed clear maxima for each magnetization jumps, and an additional change in slope at higher magnetic fields where a broad magnetization anomaly is observed (highest field). The temperature-magnetic field dependence of these features is shown in Fig. 4(c) in addition to the transition points determined from $M(T)$ and $C(T)$ curves. While at low magnetic field $B \leq 0.5$ T, only the antiferro-paramagnetic transition is observed, applying higher fields at $T < 31$ K reveals additional transition lines with two intermediate phases, which we assume are non-collinear (canted) ferromagnetic magnetic structures. These intermediate phases are notably different from the low field antiferromagnetic order, as they correspond to finite magnetization values. With increasing temperature, the critical field corresponding to the second jump (higher field) and broad anomaly (highest field) broadens and becomes indistinguishable above 21 K. Nevertheless, the two first magnetization jumps present similar evolutions of their critical fields as a function of temperature $dB_c/dT \approx -0.035$ T/K and –0.045 T/K, for the first and second jump, respectively. Due to the relative broadness of the magnetization anomalies with the increase in temperature, it is difficult to establish criteria to accurately determine their amplitude. Considering the $M(B)$ curve at 15 K (mid-way temperature between 3 and 30 K), considering a total magnetization increase (ΔM) resulting from both first and second magnetization jumps at this temperature (~15.0 μ_B/f.u.), and an average field dependence $(\partial B/\partial T)$ of −0.04 T/K, the Clausius-Clapeyron equation could allow us to estimate an overall entropy change associated with the metamagnetic behavior involving the two first discontinuous magnetization jumps (this remains an approximation as usually this formalism is employed on a single transition line): $\Delta S_{CC} = -\Delta M.(\partial B/\partial T) \approx 5.6\,J\,kg^{-1}K^{-1}$. Compared with other materials (transition entropy changes of the order of 30 J kg^{-1} K^{-1} are common among giant magnetocaloric materials [31,36]), or in comparison with

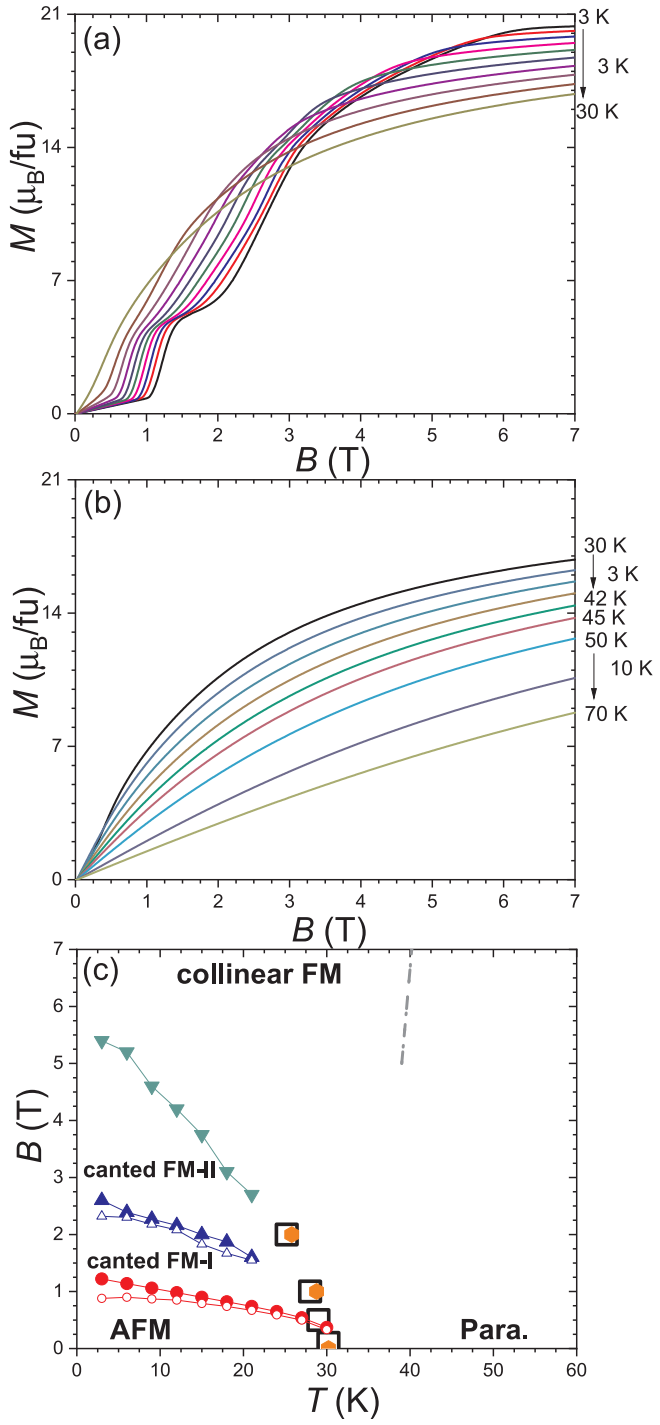

Fig. 4. Magnetic properties of $SnOEu_3$. (a) and (b) Isothermal magnetization recorded upon increasing field between 3 and 30 K using 3 K increment, and between 30 and 70 K, respectively. (c) Temperature-magnetic field dependence of the magnetization jumps observed in panel (a) upon magnetizing (filled symbols) and demagnetizing (open symbols) representing an effective magnetic phase diagram. The circles mark the first jump, the up-triangles the second, and the down-triangles the broad transition. The open squares indicate the maxima on $M(T)$ measurements, the diamond the maximum on $C(T)$, and the dash the inflection points resembling a T_C on high-field $M(T)$ curves.

the total magnetic entropy accessible to the system $S_M = 3R\ln(2J + 1) = 51.9$ J mol^{-1} K^{-1} or 87.9 J kg^{-1} K^{-1}, this transition appears relatively weak.

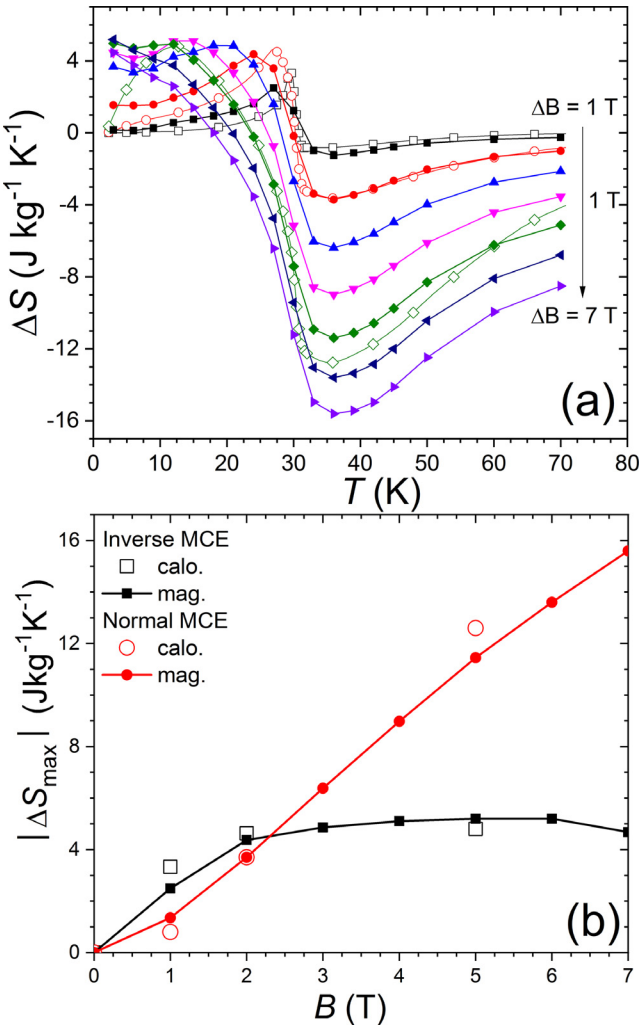

Fig. 5. Magnetocaloric effect of $SnOEu_3$. (a) Isothermal entropy changes (ΔS) derived from magnetic (closed symbols) and calorimetric (open symbols) methods. (b) Field dependence of inverse (squares) and normal (circles) MCE maxima derived from magnetization (full symbols) and calorimetry (open symbols).

3.3. Magnetocaloric effect as probe for the metamagnetic transition

The isothermal entropy changes (ΔS) of $SnOEu_3$ shown in Fig. 5 were determined using indirect magnetic and calorimetric methods based on the Maxwell equation and the isothermal difference between $S(T)$ functions obtained by integration of the heat capacity data measured in different magnetic fields, respectively. Results from both methods are in agreement. Upon heating, an inverse magnetocaloric effect at $T < 30$ K (positive ΔS values for a positive ΔB) is followed by a conventional MCE above T_N. At low temperatures, the increase in magnetic field from 2 to 7 T leads to a displacement of the inverse MCE peak towards low temperatures, but its maximum value remains nearly constant (Fig. 5b). The shape of the $\Delta S(T)$ curve at low temperatures however partially departs from the standard crenel shape expected for a first-order magnetic transition, and the crossing between the inverse and conventional MCE (the temperature at which $\Delta S = 0$) progressively shifts to lower temperatures from 30 K in 1 T to 18 K in 7 T. In addition, the maximum of the inverse ΔS shows a limited decrease at high field ($B > 6$ T). This suggests a competition between the inverse MCE from the first-order metamagnetic behavior, with the conventional MCE originating from the high-field ferromagnetic phase. For the conventional MCE, increasing the magnetic field increases the ΔS maximum, see Fig. 5b. This dependence is in line with that expected from a

paramagnet (at $T > T_N$ in low field) or a ferromagnet near its T_C (in high-field). The adiabatic temperature changes (not shown) also present a succession of the inverse and normal MCE. In $B = 2$ T, the maximum of the inverse MCE, $\Delta T_{ad} = -1.1$ K at $T = 28$ K, equals that of the normal MCE, $\Delta T_{ad} = +1.1$ K at $T = 34$ K. In contrast, in the magnetic field of 5 T, the MCE associated with the metamagnetic transition, $\Delta T_{ad} = -2.3$ K at $T = 9$ K, is significantly weaker than the conventional MCE, $\Delta T_{ad} = +3.7$ K at $T = 34$ K, even though the former occurs at lower temperature.

In $SnOEu_3$, the magnetic entropy change of the inverse MCE quickly reaches saturation, with $\Delta S = +4.9$ and $+5.2$ J kg^{-1} K^{-1} in 2 and 5 T, respectively. The normal MCE requires larger field to develop a significant MCE spread over a large temperature range with ΔS peaking at -3.7, -12 and -15.7 J kg^{-1} K^{-1} in 2, 5 and 7 T, respectively. Compared to that of transition-metal based anti-perovskites, in particular with the prototypical $GaCMn_3$ giant-MCE material [6], the inverse MCE in $SnOEu_3$ is much more limited even though it is occurring at lower temperatures. On the other hand, thanks to its high magnetization, close to 200 Am^2 kg^{-1} in $SnOEu_3$, the normal MCE in $SnOEu_3$ reaches significant values at high field (-15.7 J kg^{-1} K^{-1} in 7 T) even in absence of first-order transition. However, in the same temperature range of 30–40 K, the potential magnetic refrigeration materials with strong first-order transitions such as $ErCo_2$ ($\Delta T_{ad} = 3.0$ K and 7.4 K in 2 and 5 T, respectively) present significantly larger magnetocaloric effects [36].

In $SnOEu_3$, observing a smaller inverse MCE than the normal one is unusual, as first-order metamagnetic transitions are often believed to be the best pathway to reach large giant magnetocaloric effects. The field dependence of the maxima of inverse and normal MCE in $SnOEu_3$ shows that while the normal MCE continuously increases with the field, the inverse MCE marks a very clear saturation at $\Delta S_{saturation} = 5.2$ J kg^{-1} K^{-1} at $B \geq 2$ T. This magnetocaloric isothermal entropy change associated with the metamagnetic transition actually allows us to confirm the estimate made in the previous section, $\Delta S_{tr} \approx \Delta S_{CC} \approx \Delta S_{saturation} \approx 5.2$–$5.6$ J kg^{-1} K^{-1}.

3.4. Magnetism under pressure

To check whether a significant structural component is involved in the metamagnetic transition, and whether a ferromagnetic state can be brought to the edge of stability by external pressure, magnetic measurements were carried out at selected constant pressures up to 1.05 GPa, see Fig. 6. In low magnetic field $B = 0.1$ T, Fig. 6(a), the Néel temperature shifts to lower temperatures with pressure, in addition the incipient ferromagnetism benefits from pressure application, which results in an increase in the magnetization at $M(T)$ peak maximum. The average pressure dependence of the Néel temperature, taken as the pressure dependence of the maximum of the $M(T)$ curves, is $\partial T_N/\partial P \approx -6.7$ K/GPa. At first glance, such a shift of the Néel temperature under pressure does not appear unusual but the reports on the properties of rare-earth anti-perovskites under pressure are scarce. Transition-metal based anti-perovskite, like Mn_3GaC or Mn_3GaN were investigated under pressure [8,37], but due to the fact that the origin of the exchange interactions is sensibly different, they cannot be used for comparison purposes.

At low temperatures and high magnetic fields, Fig. 6(b), one can observe an overall decrease of the critical field of the metamagnetic transition(s) due to pressure. The critical field for the first magnetic jump $B_{c1} \approx 1.25$ T in $P = 0$ decreases at an average rate of $\partial B_{C1}/\partial P \approx -0.6$ T/GPa, the second jump at $B_{c2} \approx 2.6$ T in $P = 0$ does not show a significant pressure dependence, and the broad magnetization increase around 5.6 T in $P = 0$ shifts to lower magnetic field by about 1 T for $\Delta P = 1.05$ GPa. Using the Clausius-Clapeyron equation, $\Delta V = \Delta S_{tr}/(dP/dT_{tr})$, we roughly estimate $\Delta V/V$ in the range of -0.03% to -0.06%. The saturation magnetization is not affected by hydrostatic pressure. At the highest pressure and in high magnetic field,

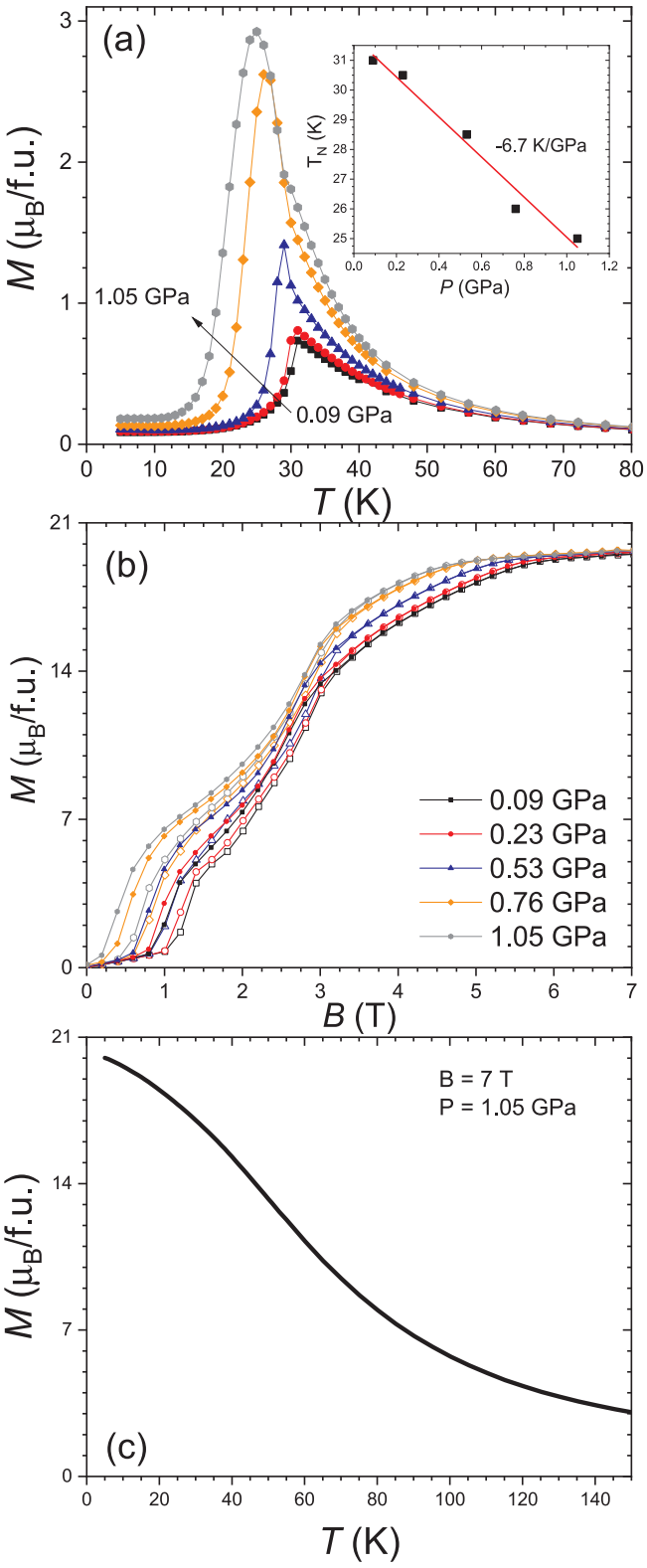

Fig. 6. Magnetism of $SnOEu_3$ under high pressure. (a) Temperature dependence of the magnetization in $B = 0.1$ T, in the inset pressure dependence of the Néel Temperature. (b) Field dependence of the magnetization in different pressures at $T = 5$ K upon magnetizing (open symbols) and demagnetizing (close symbols). (c) Temperature dependence of the magnetization in $B = 7$ T at $P = 1.05$ GPa.

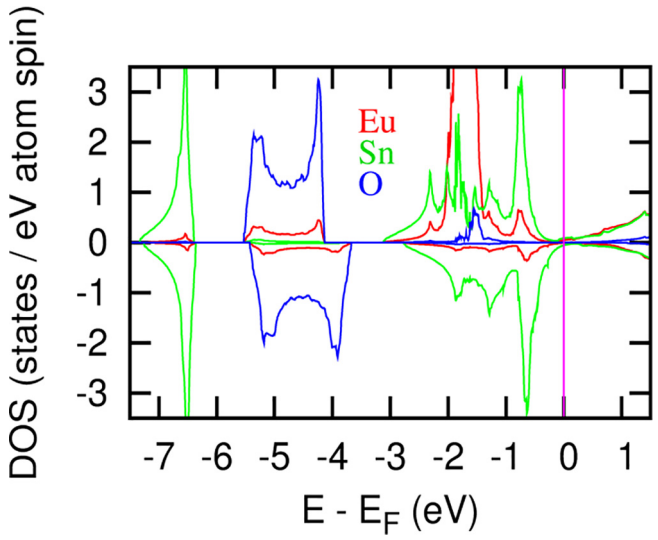

Fig. 7. Spin polarized atom projected FM density of states (DOS) of $SnOEu_3$.

Fig. 6(c), the temperature dependence of the magnetization shows a broad inflection point around 50 K, which indicates a ferromagnetic order at high field.

Overall, hydrostatic pressure is found to affect the magnetic properties of $SnOEu_3$, promoting ferromagnetism and shifting of the transition temperature. Though visible, the effect of the pressure on the metamagnetic transition remains limited suggesting that the metamagnetism is not associated with major crystallographic changes such as significant cell volume discontinuities. At the same time, it is clear that the divalent state of the Eu is stable up to 1.05 GPa. The hydrostatic pressure accessible by Cu-Be cell for magnetic measurements turned out to be insufficient to fully break the antiferromagnetic order, but our data indicate that further attempts at higher pressures could be considered.

3.5. Theoretical investigation

Fig. 7 shows the spin-polarized atom projected density of states (DOS) for ferromagnetic $SnOEu_3$. In the majority spin channel, the bottom of the conduction band is formed mainly by the fully hybridized Eu *5d* and Sn 5*p* states. The upper valence band is dominated by Eu 4*f* states peaking around −1.8 eV, hybridized with Eu 5*d*, O 2*p*, and Sn 5*p* states. The lower valence band from −4 to −5.5 eV is dominated by O 2*p* states hybridized with Eu 5*d* states. The spin minority channel shows a similar structure of the valence band, except for the Eu 4*f* states. In rare-earth compounds, localized 4*f* electrons make direct 4*f*-4*f* exchange negligible, so that the magnetic coupling usually occurs through indirect Ruderman-Kittel-Kasuya-Yosida (RKKY) exchange. The situation in $SnOEu_3$ is, however, more complicated. Considering unusual for intermetallics low DOS at and near the Fermi level, and hybridization of Eu 4*f*, 5*d* and O *2p*, as well as Eu 4*f* and 5*d* states in the valence band, suggest that a mechanism reminiscent of super-exchange plays a role in the magnetism of title compound in addition to the conventional and dominant RKKY exchange.

Table 3 shows orbital-specific magnetic moments of $SnOEu_3$ calculated from a difference between the spin up and spin down integrated DOS up to the Fermi level assuming ferromagnetic order. The *4f* magnetic moments are slightly lower than the expected 7 μ_B of Eu^{2+} ion. The small but non-negligible Eu *5d* moments are due to the overlap of Eu 4*f* and Eu 5*d* states, which is common in lanthanide intermetallic compounds. Sn develops induced moments on its *p* states, which cancel out by those on its *d* states. The induced moments on O 2*p* are antiparallel to Eu 4*f* and Eu 5*d* which, together with the super-exchange-like magnetic coupling noted above, support the antiferromagnetic

Table 3
Orbital-specific calculated magnetic moments of ferromagnetic $SnOEu_3$ (μ_B/atom).

$SnOEu_3$ (FM)	*s*	*p*	*d*	*f*
Eu	0.02	0.01	0.08	6.91
Sn	−0.01	−0.08	0.08	
O	0.00	−0.09		

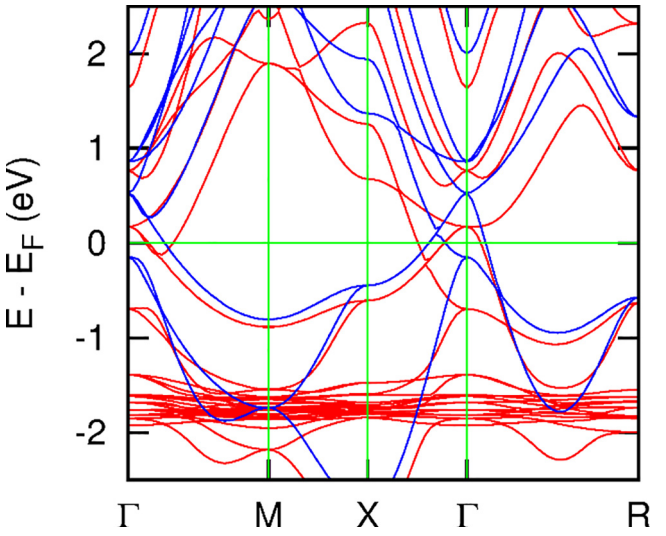

Fig. 8. Spin polarized band structure of $SnOEu_3$. The spin up (spin down) bands are represented by red (blue) color. (For interpretation of the references to colour in this figure legend, the reader is referred to the web version of this article.)

(AFM) ground state in $SnOEu_3$. As the exact type of AFM ordering is not known for this class of rare-earth anti-perovskites and considering that the low-field magnetization is particularly low at $T = 3$ K (Fig. 1), a simple antiparallel alignment of Eu magnetic moments was used to model the AFM state with three Eu moments spin up and three Eu moments spin down out of the six Eu atoms present in the 2 × 1 × 1 supercell. The total energy calculations using the 2 × 1 × 1 supercell show a difference of 52 meV/f.u. between AFM (lower energy) and FM states of $SnOEu_3$. This small energy difference between the AFM and FM ground states correlates with the instability manifested as low-field metamagnetism observed experimentally.

Fig. 8 shows spin-polarized band structure of $SnOEu_3$. As expected from the low density of electronic states near the Fermi level (E_F), only a few bands cross E_F, which indicates that $SnOEu_3$ is a semi-metal. These theoretical findings are in line with the relatively high electrical resistivity reported for $SnOEu_3$ [15]. Most band crossings are found close to the high symmetry point Γ. At the Γ point, a band inversion occurs just above the Fermi level in the spin-up channel and a semi-band inversion is observed just below the Fermi level in the spin-down channel. Unconventional band topologies near the Γ point and topological insulator behaviors have been predicted in other anti-perovskites [38,39], but in contrast to $BiNCa_3$, $SnOCa_3$ or $PbOSr_3$, $SnOEu_3$ does not have a band gap.

4. Conclusions

Stoichiometric polycrystalline $SnOEu_3$ samples were successfully prepared by melting/sintering Eu, Sn and SnO_2 reactants in tantalum using induction furnace. In line with an earlier report, an antiferromagnetic transition is observed at $T_N \approx 31$ K in low magnetic field ($B = 0.1$ T) and the application of larger magnetic fields at low temperatures reveals a metamagnetic transition toward a high

magnetization state. Discontinuous magnetization jumps are found over a broad range of temperatures between 3 and 30 K. However, the relatively slow evolution of their critical metamagnetic fields with temperature indicates a small associated latent heat, as further confirmed by heat capacity measurements as well as using the magnetocaloric effect as an indirect probe. The saturation magnetization (~20.5 μ_B/f.u.) is close to that expected for three Eu^{2+} ions and is insensitive to the external pressure up to 1.05 GPa, indicating that the Eu divalent state is quite stable in $SnOEu_3$. The critical field of the metamagnetic transition decreases with the pressure. *Ab-initio* calculations show small energy difference between ferromagnetic and antiferromagnetic grounds states, in line with the observed metamagnetism, indicate rather complex magnetic exchange mechanism, and reveal an unusual band topology at the high symmetry point (Γ) in the Brillouin zone.

CRediT authorship contribution statement

F. Guillou: Conceptualization, Investigation. **D. Paudyal:** Investigation. **Y. Mudryk:** Investigation. **A.K. Pathak:** Investigation. **V. Smetana:** Investigation. **A.-V. Mudring:** Supervision. **V.K. Pecharsky:** Supervision.

Declaration of Competing Interest

The authors declare that they have no known competing financial interests or personal relationships that could have appeared to influence the work reported in this paper.

Acknowledgments

The Ames Laboratory is operated for the U.S. Department of Energy (DOE) by Iowa State University of Science and Technology under contract No. DE-AC02-07CH11358. This work was supported by the Office of Science of the U.S. DOE, Division of Materials Sciences and Engineering, Office of Basic Energy Sciences. For the period after March 2018, F.G. thanks the support from the National Natural Science Foundation of China (grant No. 51850410514).

References

[1] V.M. Goldschmidt, Naturwissenschaften 14 (1926) 477.
[2] V.M. Goldschmidt, Geochemisce Verterlungsgesetze der Elemente, Norske Videnskap, Oslo, 1927.
[3] A.S. Bhalla, R. Guo, R. Roy, Mater. Res. Innovations 4 (2000) 3.
[4] T. He, Q. Huang, A.P. Ramirez, Y. Wang, K.A. Regan, N. Rogado, M.A. Hayward, M.K. Haas, J.S. Slusky, K. Inumara, H.W. Zandbergen, N.P. Ong, R.J. Cava, Nature 411 (2001) 54.
[5] K. Kamishima, T. Goto, H. Nakagawa, N. Miura, M. Ohashi, N. Mori, T. Sasaki, T. Kanomata, Phys. Rev. B 63 (2000) 024426.
[6] T. Tohei, H. Wada, T. Kanomata, J. Appl. Phys. 94 (2003) 1800.
[7] T. Hamada, K. Takenaka, J. Appl. Phys. 109 (2011) 07E309.
[8] D. Matsunami, A. Fujita, K. Takenaka, M. Kano, Nat. Mater. 14 (2015) 73.
[9] D. Fruchart, E.F. Bertaut, F. Sayetat, M. Nasr Eddine, R. Fruchart, J.P. Senateur, Solid State Commun. 8 (1970) 91.
[10] Y. Zhao, L.L. Daemen, J. Am. Chem. Soc. 134 (2012) 15042.
[11] M. Kosaka, Y. Uwatoko, T. Seino, H. Onodera, Phys. B 281&282 (2000) 114.
[12] J.-T. Zhao, Z.-C. Dong, J.T. Vaughey, J.E. Ostenson, J.D. Corbett, J. Alloys Compd. 230 (1995) 1.
[13] M. Kirchner, W. Schnelle, F.R. Wagner, R. Niewa, Solid State Sci. 5 (2003) 1247.
[14] T.M. Gesing, K.H. Wachtmann, W. Jeitschko, Z. Naturforsch. 52b (1997) 176.
[15] M. Kirchner, W. Schnelle, R. Niewa, Z. Anorg. Allg. Chem. 632 (2006) 559.
[16] M. Kirchner, W. Schnelle, R. Niewa, Z. Naturforsch. 61b (2006) 813.
[17] J. Nuss, C. Mühle, K. Hayama, V. Abdolazimi, H. Takagi, Acta Crystallogr. B 71 (2015) 300.
[18] A.S. Mikhaylushkin, C. Höglund, J. Birch, Zs. Czigány, L. Hultman, S.I. Simak, B. Alling, F. Tasnádi, I.A. Abrikosov, Phys. Rev. B 79 (2009) 134107.
[19] J. Rodriguez-Carvajal, Phys. B 192 (1993) 55.
[20] SMART, Bruker AXS, Inc., Madison, WI, 1996.
[21] R. Blessing, Acta Crystallogr. A 51 (1995) 33.
[22] G. Sheldrick, Acta Crystallogr. Sect. A 71 (1) (2015) 3.
[23] G. Sheldrick, Acta Crystallogr. Sect. C 71 (1) (2015) 3.
[24] V. Hardy, Y. Bréard, C. Martin, J. Phys.: Condens. Matter 21 (2009) 075403.
[25] Quantum Design, PPMS Application Note 1085-154.
[26] J. Kamarád, Z. Machátová, Z. Arnold, Rev. Sci. Instrum. 75 (2004) 5022, https://doi.org/10.1063/1.1808122.
[27] J. Thomasson, C. Ayache, I.L. Spain, M. Villedieu, J. Appl. Phys. 68 (1990) 5933, https://doi.org/10.1063/1.346924.
[28] V.I. Anisimov, F. Aryasetiawan, A.I. Lichtenstein, J. Phys.: Condens. Matter 9 (1997) 767.
[29] O.K. Andersen, O. Jepsen, Phys. Rev. Lett. 53 (1984) 2571.
[30] P. Blaha, et al., WIEN2k, An Augmented Plane Wave + Local Orbitals Program for Calculating Crystal Properties, Karlheinz Schwarz, Techn. Universität Wien, Austria, 2001.
[31] F. Guillou, A.K. Pathak, D. Paudyal, Y. Mudryk, F. Wilhelm, A. Rogalev, V.K. Pecharsky, Nat. Commun. 9 (2018) 2925.
[32] E. du Trémolet de Lacheisserie, Magnétisme, EDP Sciences, Grenoble, ISBN 2. 86883.463.9.
[33] V. Hardy, A. Wahl, C. Martin, Ch. Simon, Phys. Rev. B 63 (2001) 224403.
[34] N.V. Baranov, A.V. Proshkin, C. Czternasty, M. Meißner, A. Podlesnyak, S.M. Podgornykh, Phys. Rev. B 79 (2009) 184420.
[35] L.S. Sharath Chandra, S. Pandya, P.N. Vishwakarma, D. Jain, V. Ganesan, Phys. Rev. B 79 (2009) 052402.
[36] K.A. Gschneidner Jr., V.K. Pecharsky, A.O. Tsokol, Rep. Prog. Phys. 68 (2005) 1479.
[37] K. Kamishima, M.I. Bartashevich, T. Goto, M. Kikuchi, T. Kanomat, J. Phys. Soc. Jpn. 67 (1998) 1748.
[38] Y. Sun, X.-Q. Chen, S. Yunoki, D. Li, Y. Li, Phys. Rev. Lett. 105 (2010) 216406.
[39] T.H. Hsieh, J. Liu, L. Fu, Phys. Rev. B 90 (2014) 081112(R).